

Control Over Ligand Exchange Reactivity in Hole Transport Layer Enables High-Efficiency Colloidal Quantum Dot Solar Cells

Margherita Biondi,[#] Min-Jae Choi,[#] Seungjin Lee, Koen Bertens, Mingyang Wei, Ahmad R. Kirmani, Geonhui Lee, Hao Ting Kung, Lee J. Richter, Sjoerd Hoogland, Zheng-Hong Lu, F. Pelayo García de Arquer, and Edward H. Sargent*



Cite This: *ACS Energy Lett.* 2021, 6, 468–476



Read Online

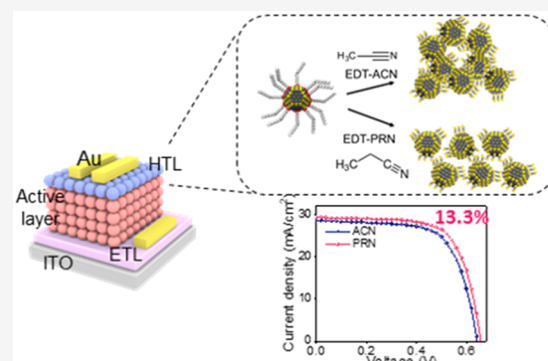
ACCESS |

Metrics & More

Article Recommendations

Supporting Information

ABSTRACT: Colloidal quantum dot (CQD) solar cells are solution-processed photovoltaic devices that exhibit promise in harvesting the infrared solar spectrum. Solid-state ligand exchange is the method employed to fabricate the CQD hole transport layer (HTL) in these cells: insulating oleic acid ligands are substituted with short thiol ligands (1,2-ethanedithiol) to create conductive p-type CQD solids. Thiols' high reactivity with the CQD surface results in rapid exchange, giving rise to aggregates of dots and unpassivated sites on dots, each contributing to sub-bandgap trap states. Here we report a strategy to minimize trap states in the CQD HTL by controlling the solvent type in the exchange. By employing a less volatile solvent, we achieve a slower reaction, leading to increased order and a 2 times reduced trap density in CQD solids. These improvements enable a power conversion efficiency of $13.1 \pm 0.1\%$ in CQD solar cells compared to control devices showing $12.4 \pm 0.1\%$.



Emerging solution-processed materials have seen intense investigation because they provide facile routes to high-performing optoelectronic devices: colloidal quantum dots (CQDs)^{1–4} for their absorption tunable across the solar spectrum; two-dimensional nanomaterials^{5–9} prized for their flexibility, transparency, and charge mobility; and organic materials¹⁰ for engineered excitonics and metal halide perovskites for outstanding transport and excited state lifetime of free electron–hole pairs.^{11,12}

CQDs have seen particular study in light-emitting diodes,^{13,14} bioimaging,¹⁵ photodetectors,^{16,17} and solar cells.^{18–21} For solar cells, lead sulfide (PbS) has received attention for its strong absorption coefficient and large Bohr radius, all relevant to light-harvesting across the solar spectrum. Advances in CQD ligand exchange and device architecture have recently enabled power conversion efficiencies (PCE) of 13%.¹⁸ PbS CQD solar cells can also complement both perovskites and c-Si in a four-terminal tandem configuration.^{22,23} Recently, CQD solar cells showed potential in flexible devices owing to their low-temperature fabrication.^{24–26}

To achieve efficient charge transport and collection in CQD solids, it is imperative to replace bulky oleic acid (OA) native ligands capping the CQDs with short conductive ligands.

Solid-state ligand exchange (SLE) is a three-step process consisting of spin coating OA CQDs on a substrate, soaking with a ligand solution, and then rinsing with solvent to eliminate the excess ligands. This procedure is employed to fabricate the hole transport layer (HTL) in state-of-art CQD solar cells, as well as in high performing field effect transistors (FET).^{19,20,27–29}

Previous studies analyzed the effects of the various interactions (CQD–CQD, CQD–solvent) within the complex SLE ligand–solvent system.^{27,29–31} The type and concentration of the ligand is crucial to the final film quality: only the right solvent–ligand balance guarantees a complete exchange without hindering the CQD surface chemistry.³⁰ The choice of solvent is also important. The optimal solvent should not hinder CQD passivation;^{27,30,32} it also should ensure solvation

Received: December 1, 2020

Accepted: December 28, 2020

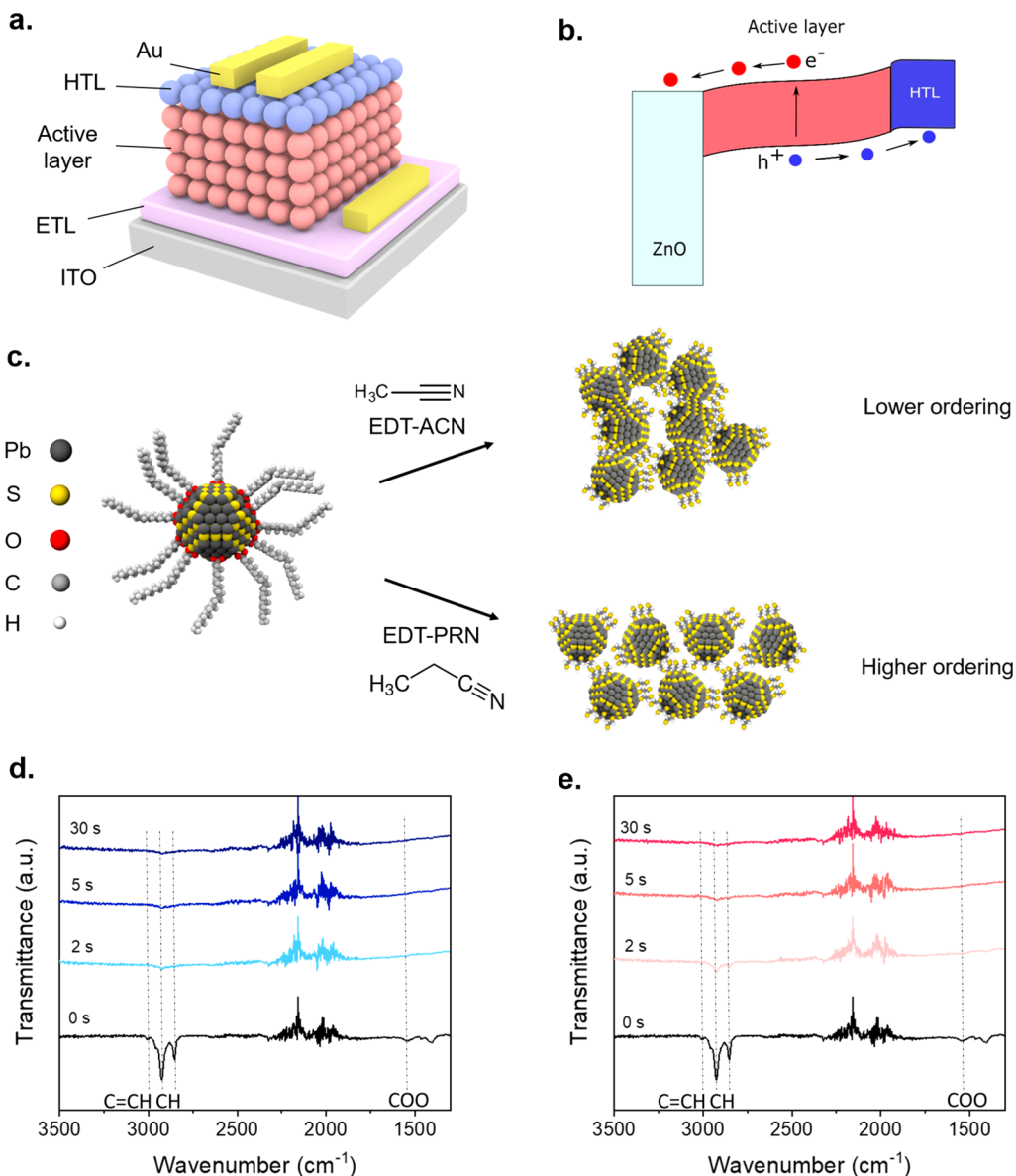


Figure 1. (a) Device structure for a standard CQD solar cell. (b) Band structure and transport of charges in a CQD solar cell after illumination. (c) Schematization of SLE for HTL. In the case of a standard solvent, the exchange is fast resulting in CQD aggregation and defects; in the case of a less volatile solvent, the exchange is slow and the structure is more ordered and with fewer defects and agglomeration. (d, e) FTIR spectra for (d) EDT-ACN and (e) EDT-PRN before exchange (0 s) and after different exchange times (2 s, 5 s, 30 s).

of the ligands, leading to increased CQD packing and enhanced mobility.²⁹

Highly polar solvents such as methanol were initially employed in the fabrication of CQD solar cells³³ and were demonstrated to enable high mobility FET devices.³⁴ However, recent studies investigating the effect of solvent polarity on the final quality of CQD solids and CQD solar cell performance revealed that highly polar solvents are detrimental to CQD passivation, resulting in defects and decreased solar cell performance. Less polar solvents such as acetonitrile (ACN) do not compromise the final CQD surface passivation and are employed in present-day CQD solar cells.³¹

We expect the solvent–ligand interaction to influence the fabrication of the HTL in state-of-art solar cells, where the exchange with 1,2-ethanedithiol (EDT) ligands, given the high reactivity of thiols,³⁵ is fast and often leads to aggregation

caused by the rapid volume contraction.^{35–37} However, the solvent's role in the SLE exchange kinetics and CQD aggregation is not fully explored and its effects, in the context of the solar cell device, are not yet fully understood.

Here we study the effect of the solvent on the SLE in terms of defects, order, and aggregation in the final film and CQD solar cell performance.

We employed propionitrile (PRN), a less volatile solvent compared to previously studied ACN, an approach to regulate the reactivity in the ligand exchange. We found that using PRN reduces CQD aggregation and defects, as shown by a 1.9 times increase in photoluminescence (PL) intensity, a 1.1 times decrease in PL half-width at half-maximum (HWHM), and a 2 times decrease in trap density. When it is applied to the fabrication of HTL for CQD solar cells, the PCE is increased ($12.4 \pm 0.1\%$ EDT-ACN HTL vs $13.1 \pm 0.1\%$ for EDT-PRN

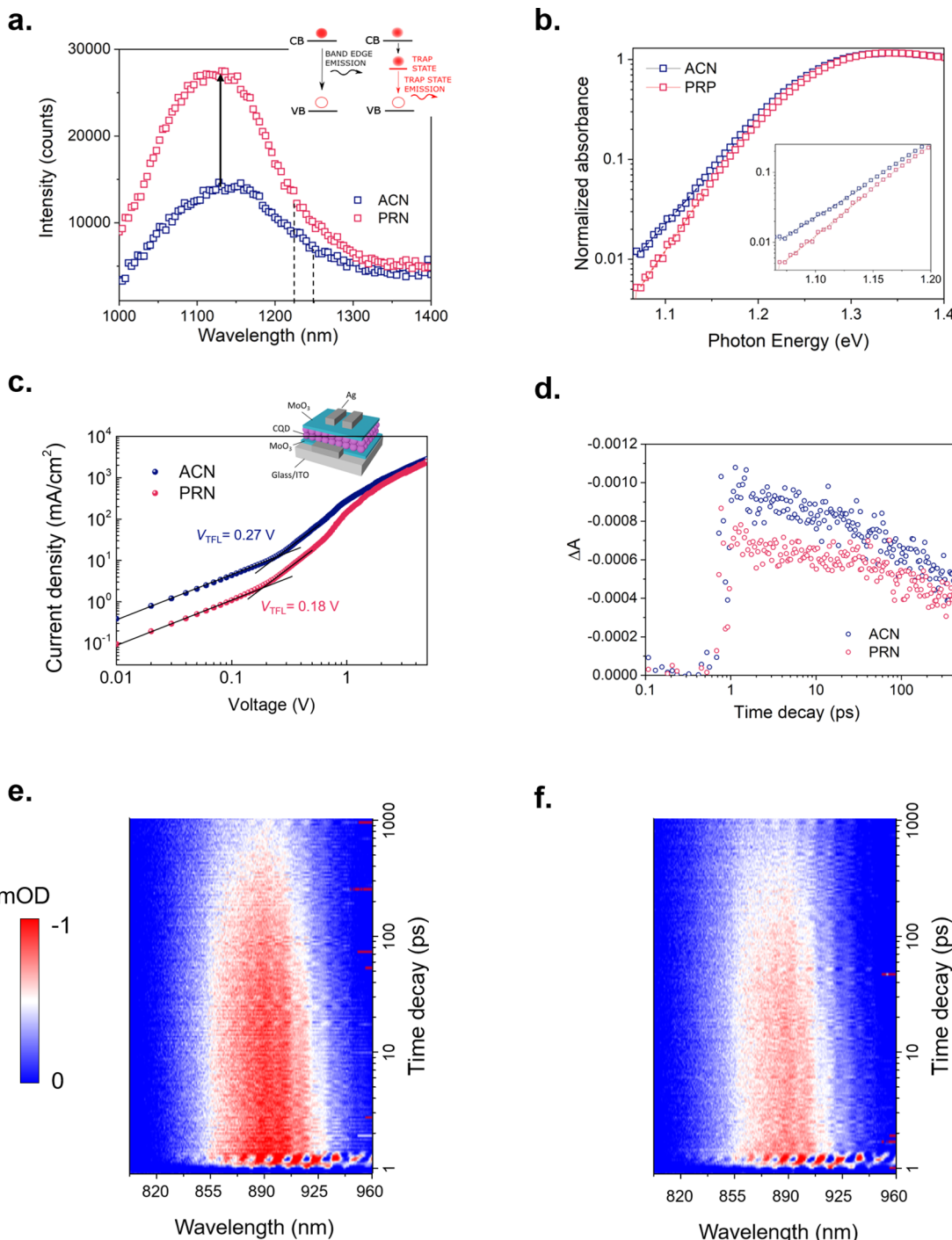


Figure 2. (a) PL spectra of EDT-ACN films and EDT-PRN films. The solid line indicates the emission center wavelength; dashed lines indicate the HWHM. The EDT-PRN shows both increased PL intensity and decreased HWHM following suppression of trap state emission and decreased agglomeration. (b) Absorbance of EDT-ACN films and EDT-PRN films, the tail of absorbance is indicative of trap states. (c) SCLC spectra for EDT-ACN and EDT-PRN hole only devices. (d) Transient absorption (TA) spectral kinetic traces of band-edge excitation bleach of EDT-ACN and EDT-PRN films pumped at 1000 nm to study shallow trap states. (e, f) TA maps for (e) EDT-ACN and (f) EDT-PRN films.

HTL); the advance arises from higher open circuit voltage (V_{OC}) and fill factor (FF) because of reduced charge recombination and improved extraction as a consequence of higher order and decreased number of defects.

State-of-art CQD solar cells consist of a n-i-p structure: transparent cathode/electron transport layer (ETL)/active layer/HTL/anode (Au) (Figure 1a). The electron–hole pairs

generated upon illumination of the active layer are collected through the charge transport layers. The HTL blocks electrons and transports holes from the active layer to the anode; in order to do this efficiently, the HTL should show p-type character (Figure 1b). A good HTL in fact should provide favorable band alignment with the active layer and minimize the defects at the active layer/HTL interface, as well as in the

HTL, responsible for unwanted recombination and decreased charge collection efficiency, leading to limited PCE.

ACN is the aprotic solvent used in the fabrication of the EDT HTL of present-day CQD solar cells, as it was shown it does not compromise the CQD surface chemistry.³¹ Nevertheless, we posited that the solvent has a key role in determining the quality of the CQD film after the EDT exchange (Figure 1c). In particular, the rapid ligand exchange in the presence of EDT–ACN can promote rapid volume shrinkage and CQD aggregation,³⁶ which might be the chief cause of disordered CQD films.

We hypothesized that a less volatile solvent could reduce the exchange reactivity. The slower evaporation and bulkier structure allow the solvent to screen the interaction between ligands and CQD surfaces during the exchange. The CQDs have time to arrange in a more ordered way since their interaction is more limited. This reduces aggregation and defects, as well as decreasing the problem of rapid contraction in film volume that leads to cracks in the final CQD solid. To this end, we employed PRN as the solvent for ligand exchange, which has more carbon than ACN, the standard solvent used for exchange.

We obtained Fourier-transform infrared (FTIR) spectra of CQD films as a function of exchange duration to study the ligand exchange speed. In the case of EDT–ACN, the CH symmetric and asymmetric stretching peaks at 3000–2800 cm⁻¹,³⁸ characteristic of OA-capped CQD films, disappear after 2 s (Figure 1d). In contrast, EDT–PRN shows the remaining CH peaks after 2 s (Figure 1e). We attribute this to a slower exchange due to the lower volatility of PRN. After 30 s of ligand exchange, both EDT–ACN and EDT–PRN achieve complete ligand exchange in the CQD films.

In order to study the solvent effect on the CQD surface chemistry, we performed X-ray photoelectron spectroscopy (XPS) on EDT–PRN and EDT–ACN exchanged films. EDT–PRN samples show a higher S/Pb atomic ratio compared to EDT–ACN (Figure S1 in Supporting Information). This agrees with improved surface passivation enabled by slower exchange. The S/Pb atomic ratio variation with exchange time shows, for EDT–PRN, an increased sulfur amount as soaking time increases, while the value is constant for EDT–ACN (Figure S1 in Supporting Information). This suggests a faster exchange in the case of EDT–ACN, in agreement with FTIR.

We performed PL measurements on the EDT exchanged films with ACN and PRN (Figure 2a). PL measurements reveal a 1.9 times increase in PL intensity for the EDT–PRN exchanged film, which can be attributed to a decreased amount of surface trap states, where charges recombine nonradiatively. The half-width at half-maximum (HWHM) of the PL emission shows a 1.1 times decrease for the EDT–PRN samples; the tail in PL at longer wavelengths is usually attributed to the formation of CQD–CQD agglomerates and trap states that favor the emission from intraband trap states at longer wavelength. We posit that the decreased HWHM may arise due to decreased agglomeration and trap states through the use of the less volatile solvent. EDT–ACN samples show a 1.1 times higher Stokes shift compared to EDT–PRN, in agreement with a higher trap density (Figure S2 in the Supporting Information).

In order to further investigate intraband trap states, we measured the absorbance of the exchanged CQD solids (Figure 2b). The slope of the absorbance in the tail region of

the spectrum is in fact indicative of localized trap states.³⁹ The EDT–PRN exchanged CQDs show a steeper slope, indicating reduced trap states.

Space-charge-limited current trap-filling measurements of hole-only devices (ITO/MoO₃/EDT–CQDs/MoO₃/Ag) were performed to quantify the trap density of the EDT-exchanged films (Figure 2c). The trap-filling region can be identified by a significant increase of current injection at a voltage ($>V_{TF}$) where all the traps are filled. The PRN-hole-only devices show lower V_{TF} (0.21 V) compared to the ACN-hole-only devices (0.18 V). The estimated trap density is $4.38 \times 10^{17} \text{ cm}^{-3}$ for ACN and $2.92 \times 10^{17} \text{ cm}^{-3}$ for PRN (details of the calculation in the Methods section in the Supporting Information). We attribute the lower trap density for EDT–PRN to the decrease in agglomerates and defects, enabled by slower exchange as a consequence of lower volatility, in agreement with PL and absorbance results.

To study the charge carrier kinetics following surface trapping, we performed ultrafast transient absorption (TA) measurements. We photoexcited the EDT–ACN and EDT–PRN samples with a sub-bandgap laser pulse (1000 nm) to excite the ground state to trap state. Figure 2d shows kinetic traces of the signal intensity at a wavelength corresponding to the CQD band-edge bleach, and panels e and f of Figure 2 show kinetic traces of the signal amplitude from 800 to 960 nm. We observe that the band-edge exciton bleach (~890 nm) appears within 5 ps after trap state excitation. This indicates population transfer from trap to the band edge, as shown in prior reports.⁴⁰ The lower signal intensity of PRN samples at short times compared to ACN samples suggests a lower defect density in the PRN sample.⁴¹

Atomic force microscope (AFM) and scanning electron microscope (SEM) measurements of the film surface reveal the effect of solvent on the morphology of the CQD solids. From AFM measurements (Figure S3 in the Supporting Information), we calculated the RMS surface roughness and found a decreased surface roughness in the case of PRN (1.6 ± 0.2 nm) compared to ACN (2.8 ± 0.4 nm). Additionally, from SEM images, we observe in the PRN sample a reduced number of cracks, caused by volume shrinkage following rapid exchange³⁷ (Figure S4 in the Supporting Information). We attribute this to the slower exchange kinetics, which minimize the rate of volume contraction.

We employed ultraviolet photoelectron spectroscopy (UPS) to investigate the solvent effect on the energy levels of the HTL and determine whether the films exchanged with different EDT–solvent combinations can work as the HTL in the final device structure. The bandgap was determined from absorption measurements, the Fermi level (E_F), and the valence band maximum (VBM) from the UPS spectrum (Figure S5 in the Supporting Information), while the conduction band minimum (CBM) was calculated from the VBM and E_g . Figure S5b shows the band energy level for EDT–ACN and EDT–PRN CQDs; we can see a shift of the position of the E_F , in particular in the case of EDT–PRN the E_F is 0.2 eV shallower compared to ACN. We note that the doping level is also influenced by the solvent, specifically the p-character increases when PRN is employed. We attribute this to a possible increased CQD passivation that leads to more thiols on the surface, and a higher difference between the vacuum energy and the Fermi level,⁴² as shown by XPS measurements.

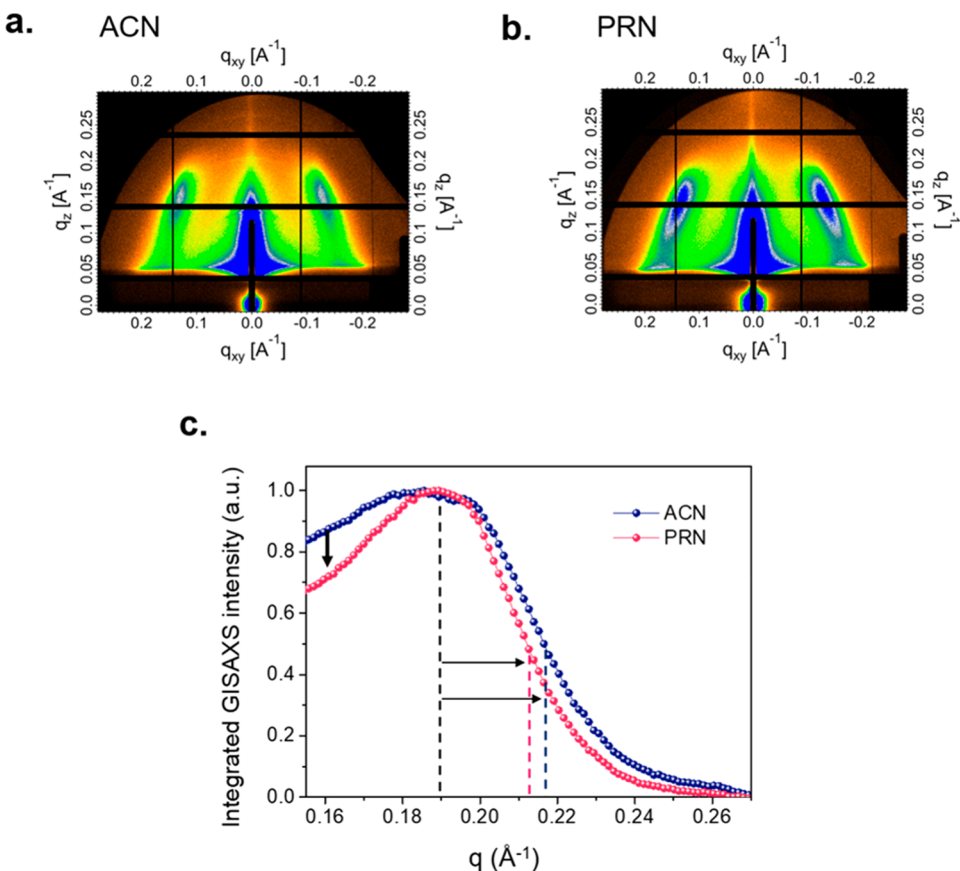


Figure 3. (a) GISAXS pattern for EDT-ACN. (b) GISAXS pattern for EDT-PRN. (c) Integrated GISAXS intensity for EDT-ACN and EDT-PRN.

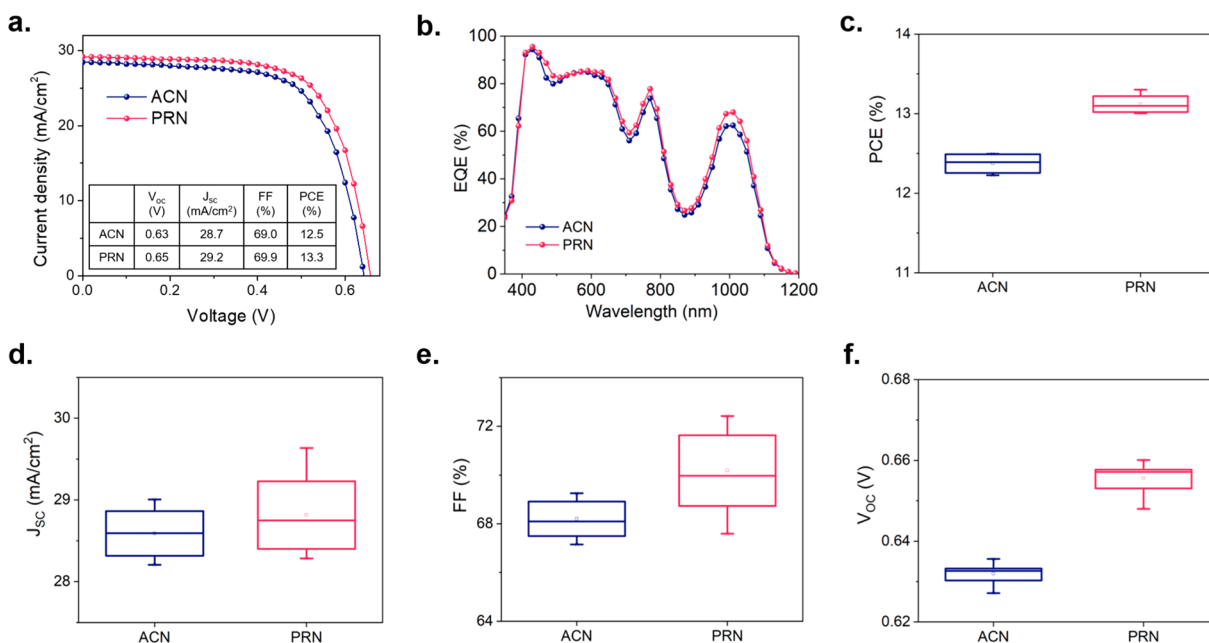


Figure 4. (a) Measured JV curves of EDT-ACN and EDT-PRN champion devices. (b) Measured EQE of EDT-ACN and EDT-PRN champion devices. Statistics on the (c) PCE, (d) J_{sc} , (e) FF, (f) V_{oc} , of EDT-ACN and EDT-PRN devices. Box and whisker plots represent the four quartiles of the distribution over a minimum of six devices. The empty square represents the mean value from the statistics.

To study the order of the exchanged films, we performed grazing-incidence small-angle X-ray scattering (GISAXS) measurements on OA capped CQDs before exchange and after exchange with EDT-ACN and EDT-PRN (Figure

3a,b). GISAXS reveals that the interdot distance decreases from 5.5 nm in the case of OA CQDs (Figure S6 in the Supporting Information) to 3.2 nm for EDT-ACN and EDT-PRN. This confirms that both ligand exchange treatments can

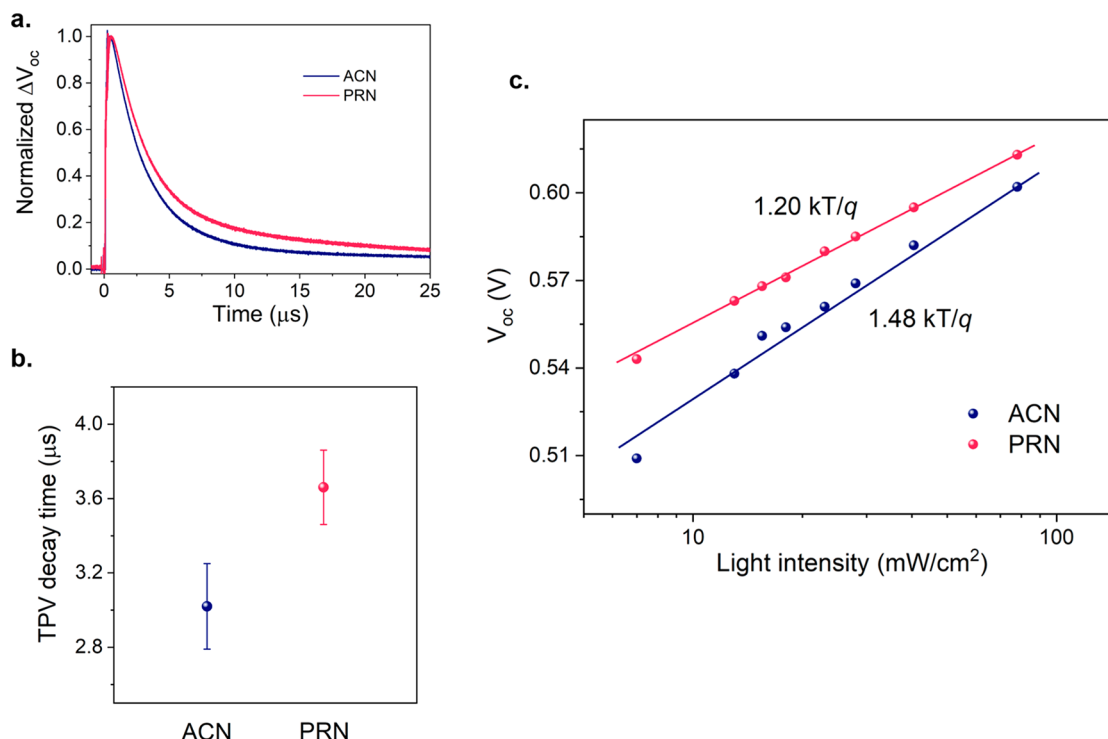


Figure 5. (a) TPV decay curves for EDT–ACN and EDT–PRN devices. (b) Average TPV decay time for EDT–ACN and EDT–PRN devices. (c) Light intensity dependent V_{oc} . The solid line is a linear fitting of the curve.

efficiently remove the OA ligands leading to closer packing, in agreement with FTIR and transmission electron microscopy (TEM) (Figure S7). The final dot-to-dot distance is similar for EDT–ACN and EDT–PRN. From the analysis of the GISAXS peaks, we observe an improvement in peak to valley (1.2 for EDT–ACN and 1.5 for EDT–PRN) and a times 1.2 decrease in HWHM, as well as an increased intensity (Figure 3c). This is indicative of more uniform packing attributed to the slower ligand exchange enabled by the use of a less volatile solvent. A more uniform packing and decrease in the density of agglomerates contributes to a reduced number of defects in the final film, as agglomeration and nonuniform ligand exchange are responsible for defects and energetic disorder in the final film.^{40,43}

In order to investigate the effect of the solvent on carrier transport, we measured conductivity on EDT–ACN and EDT–PRN CQDs (Figure S8 and S9 in the Supporting Information). EDT–PRN showed 1.3 times higher conductivity compared to EDT–ACN ($1.3 \times 10^{-3} \text{ S m}^{-1}$ for EDT–PRN and $9.8 \times 10^{-4} \text{ S m}^{-1}$ for EDT–ACN). The increased conductivity can be attributed to the improved order and decreased number of defects, in agreement with PL, SCLC, TA, absorbance, and GISAXS results.

We then fabricated CQD solar cells using EDT–ACN and EDT–PRN as the HTL to investigate the effect of the improved HTL quality on photovoltaic performance. The champion EDT–PRN device shows a PCE of 13.3%, while the best EDT–ACN shows a PCE of 12.5% (Figure 4a). Specifically, in the EDT–PRN device we observe a significant increase in V_{oc} (0.63 for EDT–ACN and 0.65 for EDT–PRN) and FF (69% for EDT–ACN and 70% for EDT–PRN). The external quantum efficiency (EQE, Figure 4b) spectra show, for the same device thickness, an increase in the EQE at the excitonic peak, as a consequence of the improved

collection efficiency in the device. The CQD absorption coefficient is in fact higher for the shorter wavelength region compared to longer wavelengths. This causes the longer wavelengths to be absorbed mainly at the back of the device (active layer/HTL interface), while shorter wavelengths are mainly absorbed at the ETL/active layer interface. For this reason, defects at the active layer/HTL interface predominantly affect the carrier collection associated with photocarriers generated using longer-wavelength spectral components.⁴⁴

Statistics on the PCE show that the enhancement is significant (Figure 4c, $12.4 \pm 0.1\%$ for EDT–ACN and $13.1 \pm 0.1\%$ for EDT–PRN; all error bars are one sample standard deviation) and comes from combination of improved short circuit current density (J_{sc}) (Figure 4d, $28.6 \pm 0.3 \text{ mA/cm}^2$ for EDT–ACN and $28.8 \pm 0.4 \text{ mA/cm}^2$), FF (Figure 4e, $68.2 \pm 0.7\%$ for EDT–ACN and $70.2 \pm 1.4\%$ for EDT–PRN), and V_{oc} (Figure 4f, $0.632 \pm 0.003 \text{ V}$ for EDT–ACN and $0.655 \pm 0.004 \text{ V}$ for EDT–PRN). The higher standard deviation in FF and J_{sc} for PRN samples does not affect the final PCE standard deviation as a lower-than-average FF goes along with a higher-than-average J_{sc} and vice versa. We attribute the advances to a combined effect of the improved order and decreased trap states enabled by the solvent effect during HTL fabrication. To check device stability, we tracked the PCE of EDT–PRN devices under continuous device operation and found that it retains more than 90% of the initial PCE after 18 h in a nitrogen atmosphere (Figure S10 in the Supporting Information).

To test more widely the solvent volatility effect, we investigated butyronitrile (BTN), which has one more carbon chain than PRN and use it as a solvent for ligand exchange during HTL fabrication. The EDT–BTN samples show a 1.5 times increase in PL intensity compared to results for EDT–

ACN (Figure S11 in the Supporting Information), similarly to EDT–PRN. We also fabricated CQD solar cells employing EDT–BTN HTL and obtained a champion PCE of 13.2% (Figure S12 in the Supporting Information). BTN devices show an increased average performance compared to ACN devices and a similar performance compared to PRN. This result shows that additional solvents less volatile than ACN are compatible with ligand exchange.

To investigate carrier recombination dynamics in the devices, we performed transient photovoltage (TPV) measurements and light-dependent V_{OC} measurements. When EDT–PRN is employed, we observe a TPV decay time longer than that for EDT–ACN (Figure 5a,b). Since the TPV decay time is determined by the recombination rate constant of electrons and holes,⁴⁵ the result indicates a slower charge recombination rate in the PRN devices.

To study charge recombination under device operation, light intensity dependent V_{OC} was analyzed (Figure 5c). The slope of the V_{OC} over the logarithm of light intensity can be used to analyze charge carrier recombination.⁴⁶ The calculated slope is $1.48 \text{ } kT/q$ for ACN devices and $1.20 \text{ } kT/q$ for PRN devices, where k , T , and q are the Boltzmann constant, temperature, and the elemental charge, respectively. The lower slope in the PRN devices suggests that the monomolecular recombination in the devices is reduced compared to the ACN devices. In addition, for a heterojunction CQD solar cell, the lower slope implies a decrease of recombination by sub-bandgap traps,^{47,48} in agreement with TA and PL results.

We also performed high dynamic range (HDR) EQE on ACN and PRN devices (Figure S13 in the Supporting Information) to reveal additional information on the trap state density in the final device. The spectra show a decreased tail in the HDR EQE for PRN devices, in agreement with a decreased number of trap states, as shown by PL, absorbance, SCLC, and TA measurements.

We studied the variation of device performance with ligand exchange time and HTL thickness, observing a strong dependence of V_{OC} on these parameters. When the exchange is shorter than the optimum time (30 s), we observe decreased V_{OC} as a consequence of incomplete ligand exchange, which causes the rise of defects, the chief cause of V_{OC} losses.^{20,49} In particular, we observe a stronger decrease of V_{OC} from 5 s to 2 s for the EDT–PRN device, we attribute this to the lower EDT–PRN reactivity and slower exchange, that results in a more incomplete exchange at 2 s compared to ACN, in agreement with FTIR and XPS (Figure S14a in the Supporting Information). Exchange longer than 30 s is not investigated, as thiols can compromise the chemistry of the underlying active layer during soaking.

A similar trend is observed with thickness variation (Figure S14b in the Supporting Information): when the HTL thickness is thinner than the standard value ($\sim 60 \text{ nm}$), V_{OC} is reduced. We hypothesize this is caused by insufficient depletion region between active layer and HTL. When the HTL is thicker ($\sim 100 \text{ nm}$), the increased series resistance results in a decrease of V_{OC} .⁵⁰ A variation in CQD concentration in HTL fabrication also results in thickness variation and a similar V_{OC} trend with the above HTL thickness studies (Figures S14c and S15 in the Supporting Information).

In sum, we investigated the effect of solvent choice during the SLE of HTL for CQD solar cells and found that a less volatile solvent increases the CQD order, increases passivation, and decreases defects and agglomeration. Further insight into

trapping and detrapping kinetics in SLE and the effect of solvent volatility could be obtained by employing thermal admittance spectroscopy⁵¹ and terahertz mobility measurements.^{52,53} These improvements result in an increased PCE for CQD solar cells and yield further understanding of the CQD SLE process and optimization.

ASSOCIATED CONTENT

Supporting Information

The Supporting Information is available free of charge at <https://pubs.acs.org/doi/10.1021/acsenergylett.0c02500>.

Experimental details of synthesis of CQDs, synthesis of CQD inks, fabrication of CQD solar cells, and characterizations ($J-V$, EQE, PL, absorption measurement, UPS, GISAXS, conductivity, FTIR, SCLC, TEM, AFM, TA, TPV); additional figures of GISAXS, conductivity, FTIR, XPS, AFM, TEM, SEM, HDR EQE (PDF)

AUTHOR INFORMATION

Corresponding Author

Edward H. Sargent – Department of Electrical and Computer Engineering, University of Toronto, Toronto, Ontario MSS 3G4, Canada;  orcid.org/0000-0003-0396-6495; Email: ted.sargent@utoronto.ca

Authors

Margherita Biondi – Department of Electrical and Computer Engineering, University of Toronto, Toronto, Ontario MSS 3G4, Canada

Min-Jae Choi – Department of Electrical and Computer Engineering, University of Toronto, Toronto, Ontario MSS 3G4, Canada;  orcid.org/0000-0002-6699-1703

Seungjin Lee – Department of Electrical and Computer Engineering, University of Toronto, Toronto, Ontario MSS 3G4, Canada;  orcid.org/0000-0002-6318-0702

Koen Bertens – Department of Electrical and Computer Engineering, University of Toronto, Toronto, Ontario MSS 3G4, Canada;  orcid.org/0000-0002-2701-1397

Mingyang Wei – Department of Electrical and Computer Engineering, University of Toronto, Toronto, Ontario MSS 3G4, Canada

Ahmad R. Kirmani – Materials Science and Engineering Division, National Institute of Standards and Technology (NIST), Gaithersburg, Maryland 20899, United States;  orcid.org/0000-0002-8351-3762

Geonhui Lee – Department of Electrical and Computer Engineering, University of Toronto, Toronto, Ontario MSS 3G4, Canada

Hao Ting Kung – Department of Materials Science and Engineering, University of Toronto, Toronto, ON MSS 3E4, Canada

Lee J. Richter – Materials Science and Engineering Division, National Institute of Standards and Technology (NIST), Gaithersburg, Maryland 20899, United States;  orcid.org/0000-0002-9433-3724

Sjoerd Hoogland – Department of Electrical and Computer Engineering, University of Toronto, Toronto, Ontario MSS 3G4, Canada;  orcid.org/0000-0002-3099-585X

Zheng-Hong Lu – Department of Materials Science and Engineering, University of Toronto, Toronto, ON MSS 3E4, Canada;  orcid.org/0000-0003-2050-0822

F. Pelayo García de Arquer – Department of Electrical and Computer Engineering, University of Toronto, Toronto, Ontario M5S 3G4, Canada; orcid.org/0000-0003-2422-6234

Complete contact information is available at:
<https://pubs.acs.org/10.1021/acsenergylett.0c02500>

Author Contributions

#M. Biondi and M.-J. Choi contributed equally to this work.

Notes

The authors declare no competing financial interest.

¶(A.R.K.) Guest researcher.

ACKNOWLEDGMENTS

This work was supported by the Ontario Research Fund-Research Excellence program (ORF7 ministry of Research and Innovation, Ontario Research Fund-Research Excellence Round 7) and by the Natural Sciences and Engineering Research Council (NSERC) of Canada. This work was also supported by the Dongguk University Research Fund of 2020. The authors acknowledge the financial support from QD Solar. This research used resources of the National Synchrotron Light Source II, which are U.S. DOE Office of Science Facilities, at Brookhaven National Laboratory under contract no. DE-SC0012704. We thank D. Kopilovic, E. Palmiano, L. Levina, and R. Wolowiec for the technical support.

REFERENCES

- (1) Hines, M. A.; Scholes, G. D. Colloidal PbS Nanocrystals with Size-Tunable Near-Infrared Emission: Observation of Post-Synthesis Self-Narrowing of the Particle Size Distribution. *Adv. Mater.* **2003**, *15* (21), 1844–1849.
- (2) Moreels, I.; Justo, Y.; De Geyter, B.; Haustraete, K.; Martins, J. C.; Hens, Z. Size-Tunable, Bright, and Stable PbS Quantum Dots: A Surface Chemistry Study. *ACS Nano* **2011**, *5* (3), 2004–2012.
- (3) Kovalenko, M. V.; Manna, L.; Cabot, A.; Hens, Z.; Talapin, D. V.; Kagan, C. R.; Klimov, V. I.; Rogach, A. L.; Reiss, P.; Milliron, D. J.; Guyot-Sionnest, P.; Konstantatos, G.; Parak, W. J.; Heyeon, T.; Korgel, B. A.; Murray, C. B.; Heiss, W. Prospects of Nanoscience with Nanocrystals. *ACS Nano* **2015**, *9* (2), 1012–1057.
- (4) Choi, H.; Ko, J. H.; Kim, Y. H.; Jeong, S. Steric-Hindrance-Driven Shape Transition in PbS Quantum Dots: Understanding Size-Dependent Stability. *J. Am. Chem. Soc.* **2013**, *135* (14), 5278–5281.
- (5) Kufer, D.; Nikitskiy, I.; Lasanta, T.; Navickaite, G.; Koppens, F. H. L.; Konstantatos, G. Hybrid 2D-0D MoS₂-PbS Quantum Dot Photodetectors. *Adv. Mater.* **2015**, *27* (1), 176–180.
- (6) Huang, Z.; Han, W.; Tang, H.; Ren, L.; Chander, D. S.; Qi, X.; Zhang, H. Photoelectrochemical-Type Sunlight Photodetector Based on MoS₂/ Graphene Heterostructure. *2D Mater.* **2015**, *2* (3), 035011.
- (7) Xing, C.; Huang, W.; Xie, Z.; Zhao, J.; Ma, D.; Fan, T.; Liang, W.; Ge, Y.; Dong, B.; Li, J.; Zhang, H. Ultrasmall Bismuth Quantum Dots: Facile Liquid-Phase Exfoliation, Characterization, and Application in High-Performance UV-Vis Photodetector. *ACS Photonics* **2018**, *5* (2), 621–629.
- (8) Jiang, X.; Kuklin, A. V.; Baev, A.; Ge, Y.; Ågren, H.; Zhang, H.; Prasad, P. N. Two-Dimensional MXenes: From Morphological to Optical, Electric, and Magnetic Properties and Applications. *Phys. Rep.* **2020**, *848*, 1–58.
- (9) Guo, S.; Zhang, Y.; Ge, Y.; Zhang, S.; Zeng, H.; Zhang, H. 2D V-V Binary Materials: Status and Challenges. *Adv. Mater.* **2019**, *31* (39), 1902352.
- (10) Hou, J.; Inganás, O.; Friend, R. H.; Gao, F. Organic Solar Cells Based on Non-Fullerene Acceptors. *Nat. Mater.* **2018**, *17* (2), 119–128.
- (11) Meng, L.; You, J.; Yang, Y. Addressing the Stability Issue of Perovskite Solar Cells for Commercial Applications. *Nat. Commun.* **2018**, *9* (1), 5265.
- (12) Li, Z.; Klein, T. R.; Kim, D. H.; Yang, M.; Berry, J. J.; Van Hest, M. F. A. M.; Zhu, K. Scalable Fabrication of Perovskite Solar Cells. *Nat. Rev. Mater.* **2018**, *3*, 18017.
- (13) Vasilopoulou, M.; Kim, H. P.; Kim, B. S.; Papadakis, M.; Ximim Gavim, A. E.; Macedo, A. G.; Jose da Silva, W.; Schneider, F. K.; Mat Teridi, M. A.; Coutsolelos, A. G.; bin Mohd Yusoff, A. R. Efficient Colloidal Quantum Dot Light-Emitting Diodes Operating in the Second near-Infrared Biological Window. *Nat. Photonics* **2020**, *14* (1), 50–56.
- (14) Wijaya, H.; Darwan, D.; Zhao, X.; Ong, E. W. Y.; Lim, K. R. G.; Wang, T.; Lim, L. J.; Khoo, K. H.; Tan, Z. K. Efficient Near-Infrared Light-Emitting Diodes Based on In(Zn)As-In(Zn)P-GaP-ZnS Quantum Dots. *Adv. Funct. Mater.* **2020**, *30* (4), 1906483.
- (15) Omogo, B.; Gao, F.; Bajwa, P.; Kaneko, M.; Heyes, C. D. Reducing Blinking in Small Core-Multishell Quantum Dots by Carefully Balancing Confinement Potential and Induced Lattice Strain: The “Goldilocks” Effect. *ACS Nano* **2016**, *10* (4), 4072–4082.
- (16) Clifford, J. P.; Konstantatos, G.; Johnston, K. W.; Hoogland, S.; Levina, L.; Sargent, E. H. Fast, Sensitive and Spectrally Tuneable Colloidal-Quantum-Dot Photodetectors. *Nat. Nanotechnol.* **2009**, *4* (1), 40–44.
- (17) Gao, J.; Nguyen, S. C.; Bronstein, N. D.; Alivisatos, A. P. Solution-Processed, High-Speed, and High-Quantum-Efficiency Quantum Dot Infrared Photodetectors. *ACS Photonics* **2016**, *3* (7), 1217–1222.
- (18) Choi, M. J.; García de Arquer, F. P.; Proppe, A. H.; Seifitokaldani, A.; Choi, J.; Kim, J.; Baek, S. W.; Liu, M.; Sun, B.; Biondi, M.; Scheffel, B.; Walters, G.; Nam, D. H.; Jo, J. W.; Ouellette, O.; Voznyy, O.; Hoogland, S.; Kelley, S. O.; Jung, Y. S.; Sargent, E. H. Cascade Surface Modification of Colloidal Quantum Dot Inks Enables Efficient Bulk Homojunction Photovoltaics. *Nat. Commun.* **2020**, *11* (1), 103.
- (19) Aqoma, H.; Al Mubarok, M.; Hadromo, W. T.; Lee, E. H.; Kim, T. W.; Ahn, T. K.; Oh, S. H.; Jang, S. Y. High-Efficiency Photovoltaic Devices Using Trap-Controlled Quantum-Dot Ink Prepared via Phase-Transfer Exchange. *Adv. Mater.* **2017**, *29* (19), 1605756.
- (20) Pradhan, S.; Stavrinadis, A.; Gupta, S.; Christodoulou, S.; Konstantatos, G. Breaking the Open-Circuit Voltage Deficit Floor in PbS Quantum Dot Solar Cells through Synergistic Ligand and Architecture Engineering. *ACS Energy Lett.* **2017**, *2* (6), 1444–1449.
- (21) Xue, Y.; Yang, F.; Yuan, J.; Zhang, Y.; Gu, M.; Xu, Y.; Ling, X.; Wang, Y.; Li, F.; Zhai, T.; Li, J.; Cui, C.; Chen, Y.; Ma, W. Toward Scalable PbS Quantum Dot Solar Cells Using a Tailored Polymeric Hole Conductor. *ACS Energy Lett.* **2019**, *4* (12), 2850–2858.
- (22) Karani, A.; Yang, L.; Bai, S.; Futscher, M. H.; Snaith, H. J.; Ehrler, B.; Greenham, N. C.; Di, D. Perovskite/Colloidal Quantum Dot Tandem Solar Cells: Theoretical Modeling and Monolithic Structure. *ACS Energy Lett.* **2018**, *3* (4), 869–874.
- (23) Chen, B.; Baek, S. W.; Hou, Y.; Aydin, E.; De Bastiani, M.; Scheffel, B.; Proppe, A.; Huang, Z.; Wei, M.; Wang, Y. K.; Jung, E. H.; Allen, T. G.; Van Kerschaver, E.; García de Arquer, F. P.; Saidaminov, M. I.; Hoogland, S.; De Wolf, S.; Sargent, E. H. Enhanced Optical Path and Electron Diffusion Length Enable High-Efficiency Perovskite Tandems. *Nat. Commun.* **2020**, *11* (1), 1257.
- (24) Choi, M. J.; Kim, Y. J.; Lim, H.; Alarousu, E.; Adhikari, A.; Shaheen, B. S.; Kim, Y. H.; Mohammed, O. F.; Sargent, E. H.; Kim, J. Y.; Jung, Y. S. Tuning Solute-Redistribution Dynamics for Scalable Fabrication of Colloidal Quantum-Dot Optoelectronics. *Adv. Mater.* **2019**, *31* (32), 1970225.
- (25) Cho, Y.; Giraud, P.; Hou, B.; Lee, Y. W.; Hong, J.; Lee, S.; Pak, S.; Lee, J.; Jang, J. E.; Morris, S. M.; Sohn, J. I.; Cha, S. N.; Kim, J. M. Charge Transport Modulation of a Flexible Quantum Dot Solar Cell Using a Piezoelectric Effect. *Adv. Energy Mater.* **2018**, *8* (3), 1700809.
- (26) Zhang, X.; Santra, P. K.; Tian, L.; Johansson, M. B.; Rensmo, H.; Johansson, E. M. J. Highly Efficient Flexible Quantum Dot Solar

- Cells with Improved Electron Extraction Using MgZnO Nanocrystals. *ACS Nano* **2017**, *11* (8), 8478–8487.
- (27) Lu, K.; Wang, Y.; Liu, Z.; Han, L.; Shi, G.; Fang, H.; Chen, J.; Ye, X.; Chen, S.; Yang, F.; Shulga, A. G.; Wu, T.; Gu, M.; Zhou, S.; Fan, J.; Loi, M. A.; Ma, W. High-Efficiency PbS Quantum-Dot Solar Cells with Greatly Simplified Fabrication Processing via “Solvent-Curing. *Adv. Mater.* **2018**, *30* (25), 1707572.
- (28) Zarghami, M. H.; Liu, Y.; Gibbs, M.; Gebremichael, E.; Webster, C.; Law, M. P-Type PbSe and PbS Quantum Dot Solids Prepared with Short-Chain Acids and Diacids. *ACS Nano* **2010**, *4* (4), 2475–2485.
- (29) Liu, L.; Bisri, S. Z.; Ishida, Y.; Hashizume, D.; Aida, T.; Iwasa, Y. Ligand and Solvent Effects on Hole Transport in Colloidal Quantum Dot Assemblies for Electronic Devices. *ACS Appl. Nano Mater.* **2018**, *1* (9), 5217–5225.
- (30) Kirmani, A. R.; Walters, G.; Kim, T.; Sargent, E. H.; Amassian, A. Optimizing Solid-State Ligand Exchange for Colloidal Quantum Dot Optoelectronics: How Much Is Enough? *ACS Appl. Energy Mater.* **2020**, *3* (6), 5385–5392.
- (31) Kirmani, A. R.; Carey, G. H.; Abdelsamie, M.; Yan, B.; Cha, D.; Rollny, L. R.; Cui, X.; Sargent, E. H.; Amassian, A. Effect of Solvent Environment on Colloidal-Quantum-Dot Solar-Cell Manufacturability and Performance. *Adv. Mater.* **2014**, *26* (27), 4717–4723.
- (32) Pattantyus-Abram, A. G.; Kramer, I. J.; Barkhouse, A. R.; Wang, X.; Konstantatos, G.; Debnath, R.; Levina, L.; Raabe, I.; Nazeeruddin, M. K.; Grätzel, M.; Sargent, E. H. Depleted-Heterojunction Colloidal Quantum Dot Solar Cells. *ACS Nano* **2010**, *4* (6), 3374–3380.
- (33) Ip, A. H.; Thon, S. M.; Hoogland, S.; Voznyy, O.; Zhitomirsky, D.; Debnath, R.; Levina, L.; Rollny, L. R.; Carey, G. H.; Fischer, A.; Kemp, K. W.; Kramer, I. J.; Ning, Z.; Labelle, A. J.; Chou, K. W.; Amassian, A.; Sargent, E. H. Hybrid Passivated Colloidal Quantum Dot Solids. *Nat. Nanotechnol.* **2012**, *7* (9), 577–582.
- (34) Bisri, S. Z.; Piliego, C.; Yarema, M.; Heiss, W.; Loi, M. A. Low Driving Voltage and High Mobility Ambipolar Field-Effect Transistors with PbS Colloidal Nanocrystals. *Adv. Mater.* **2013**, *25* (31), 4309–4314.
- (35) Giansante, C.; Carbone, L.; Giannini, C.; Altamura, D.; Ameer, Z.; Maruccio, G.; Lojudice, A.; Belviso, M. R.; Cozzoli, P. D.; Rizzo, A.; Gigli, G. Colloidal Arenethiolate-Capped PbS Quantum Dots: Optoelectronic Properties, Self-Assembly, and Application in Solution-Cast Photovoltaics. *J. Phys. Chem. C* **2013**, *117* (25), 13305–13317.
- (36) Aqoma, H.; Jang, S. Y. Solid-State-Ligand-Exchange Free Quantum Dot Ink-Based Solar Cells with an Efficiency of 10.9%. *Energy Environ. Sci.* **2018**, *11* (6), 1603–1609.
- (37) Lee, S.; Choi, M. J.; Sharma, G.; Biondi, M.; Chen, B.; Baek, S. W.; Najarian, A. M.; Vafaie, M.; Wicks, J.; Sagar, L. K.; Hoogland, S.; de Arquer, F. P. G.; Voznyy, O.; Sargent, E. H. Orthogonal Colloidal Quantum Dot Inks Enable Efficient Multilayer Optoelectronic Devices. *Nat. Commun.* **2020**, *11* (1), 4814.
- (38) Luther, J. M.; Law, M.; Song, Q.; Perkins, C. L.; Beard, M. C.; Nozik, A. J. Structural, Optical, and Electrical Properties of Self-Assembled Films of PbSe Nanocrystals Treated with 1,2-Ethanedithiol. *ACS Nano* **2008**, *2* (2), 271–280.
- (39) John, S.; Soukoulis, C.; Cohen, M. H.; Economou, E. N. Theory of Electron Band Tails and the Urbach Optical-Absorption Edge. *Phys. Rev. Lett.* **1986**, *57* (14), 1777–1780.
- (40) Gilmore, R. H.; Liu, Y.; Shcherbakov-Wu, W.; Dahod, N. S.; Lee, E. M. Y.; Weidman, M. C.; Li, H.; Jean, J.; Bulović, V.; Willard, A. P.; Grossman, J. C.; Tisdale, W. A. Epitaxial Dimers and Auger-Assisted Detrapping in PbS Quantum Dot Solids. *Matter* **2019**, *1* (1), 250–265.
- (41) Sun, B.; Vafaie, M.; Levina, L.; Wei, M.; Dong, Y.; Gao, Y.; Kung, H. T.; Biondi, M.; Proppe, A. H.; Chen, B.; Choi, M.-J.; Sagar, L. K.; Voznyy, O.; Kelley, S. O.; Laquai, F.; Lu, Z.-H.; Hoogland, S.; García de Arquer, F. P.; Sargent, E. H. Ligand-Assisted Reconstruction of Colloidal Quantum Dots Decreases Trap State Density. *Nano Lett.* **2020**, *20* (5), 3694–3702.
- (42) Kim, D.; Kim, D. H.; Lee, J. H.; Grossman, J. C. Impact of Stoichiometry on the Electronic Structure of PbS Quantum Dots. *Phys. Rev. Lett.* **2013**, *110* (19), 196802.
- (43) Liu, M.; Voznyy, O.; Sabatini, R.; García De Arquer, F. P.; Munir, R.; Balawi, A. H.; Lan, X.; Fan, F.; Walters, G.; Kirmani, A. R.; Hoogland, S.; Laquai, F.; Amassian, A.; Sargent, E. H. Hybrid Organic-Inorganic Inks Flatten the Energy Landscape in Colloidal Quantum Dot Solids. *Nat. Mater.* **2017**, *16* (2), 258–263.
- (44) Biondi, M.; Choi, M. J.; Ouellette, O.; Baek, S. W.; Todorović, P.; Sun, B.; Lee, S.; Wei, M.; Li, P.; Kirmani, A. R.; Sagar, L. K.; Richter, L. J.; Hoogland, S.; Lu, Z. H.; García de Arquer, F. P.; Sargent, E. H. A Chemically Orthogonal Hole Transport Layer for Efficient Colloidal Quantum Dot Solar Cells. *Adv. Mater.* **2020**, *32* (17), 1906199.
- (45) O'Regan, B. C.; Scully, S.; Mayer, A. C.; Palomares, E.; Durrant, J. The Effect of Al₂O₃ Barrier Layers in TiO₂/Dye/CuSCN Photovoltaic Cells Explored by Recombination and DOS Characterization Using Transient Photovoltaic Measurements. *J. Phys. Chem. B* **2005**, *109* (10), 4616–4623.
- (46) Kyaw, A. K. K.; Wang, D. H.; Wynands, D.; Zhang, J.; Nguyen, T. Q.; Bazan, G. C.; Heeger, A. J. Improved Light Harvesting and Improved Efficiency by Insertion of an Optical Spacer (ZnO) in Solution-Processed Small-Molecule Solar Cells. *Nano Lett.* **2013**, *13* (8), 3796–3801.
- (47) Pradhan, S.; Stavrinidis, A.; Gupta, S.; Bi, Y.; Di Stasio, F.; Konstantatos, G. Trap-State Suppression and Improved Charge Transport in PbS Quantum Dot Solar Cells with Synergistic Mixed-Ligand Treatments. *Small* **2017**, *13* (21), 1700598.
- (48) Zhang, X.; Zhang, J.; Phuylal, D.; Du, J.; Tian, L.; Öberg, V. A.; Johansson, M. B.; Cappel, U. B.; Karis, O.; Liu, J.; Rensmo, H.; Boschloo, G.; Johansson, E. M. J. Inorganic CsPbI₃ Perovskite Coating on PbS Quantum Dot for Highly Efficient and Stable Infrared Light Converting Solar Cells. *Adv. Energy Mater.* **2018**, *8* (6), 1702049.
- (49) Chuang, C. H. M.; Maurano, A.; Brandt, R. E.; Hwang, G. W.; Jean, J.; Buonassisi, T.; Bulović, V.; Bawendi, M. G. Open-Circuit Voltage Deficit, Radiative Sub-Bandgap States, and Prospects in Quantum Dot Solar Cells. *Nano Lett.* **2015**, *15* (5), 3286–3294.
- (50) Choi, M. J.; Kim, S.; Lim, H.; Choi, J.; Sim, D. M.; Yim, S.; Ahn, B. T.; Kim, J. Y.; Jung, Y. S. Highly Asymmetric N+p Heterojunction Quantum-Dot Solar Cells with Significantly Improved Charge-Collection Efficiencies. *Adv. Mater.* **2016**, *28* (9), 1780–1787.
- (51) Wang, S.; Kaienburg, P.; Klingebiel, B.; Schillings, D.; Kirchartz, T. Understanding Thermal Admittance Spectroscopy in Low-Mobility Semiconductors. *J. Phys. Chem. C* **2018**, *122* (18), 9795–9803.
- (52) Sanehira, E. M.; Marshall, A. R.; Christians, J. A.; Harvey, S. P.; Ciesielski, P. N.; Wheeler, L. M.; Schulz, P.; Lin, L. Y.; Beard, M. C.; Luther, J. M. Enhanced Mobility CsPbI₃ Quantum Dot Arrays for Record-Efficiency, High-Voltage Photovoltaic Cells. *Sci. Adv.* **2017**, *3* (10), No. eaao4204.
- (53) Talgorn, E.; Gao, Y.; Aerts, M.; Kunnen, L. T.; Schins, J. M.; Savenije, T. J.; Van Huis, M. A.; Van Der Zant, H. S. J.; Houtepen, A. J.; Siebbeles, L. D. A. Unity Quantum Yield of Photogenerated Charges and Band-like Transport in Quantum-Dot Solids. *Nat. Nanotechnol.* **2011**, *6* (11), 733–739.